Anisotropic properties of gas transport in non-woven gas diffusion layers of polymer electrolyte fuel cells

Dieter Froning^a, Monika Drakselová^b, Anna Tocháčková^b, Roman Kodým^b, Uwe Reimer^a, Werner Lehnert^{a,c,d}, Karel Bouzek^b

^aForschungszentrum Jülich GmbH, Institute of Energy and Climate Research, IEK-14:
 Electrochemical Process Engineering, D-52425 Jülich, Germany
 ^bUniversity of Chemistry and Technology, Prague, Czech Republic
 ^cModeling in Electrochemical Process Engineering, RWTH Aachen University, Germany
 ^dJARA-HPC, D-52425 Jülich, Germany

Abstract

For this study, gas transport in the gas diffusion layers of polymer electrolyte fuel cells was analyzed in one through-plane and two in-plane directions. Gas transport was calculated using Lattice Boltzmann simulations, with non-woven gas diffusion layers measured both through-plane and in-plane. The micro structure for the transport simulations was based on a stochastic model that can take into account uncompressed and compressed materials. The micro structure of this kind of gas diffusion layers is superposed by fiber bundles. Their impact on the anisotropy of the in-plane permeabilities was then investigated. Finally, the influence of structural inhomogeneities on in-plane flow was analyzed. Compression has a high influence on through-plane and in-plane permeability. The impact of the fibers bundles is smaller than the impact of local variations of the micro structure according to the stochastic geometry model.

Keywords: PEFC, GDL, Lattice Boltzmann, Experimental validation

1. Introduction

In proton exchange membrane fuel cells (PEMFCs), the gas diffusion layer (GDL) is a key component in the task of distributing the feeding gases – hydro-

 $Email\ address:\ {\tt d.froning@fz-juelich.de}\ ({\tt Dieter}\ {\tt Froning})$

gen on the anode side and oxygen on the cathode side – homogeneously across the membrane electrode assembly (MEA). In various cell and stack simulations, material properties, typically through-plane and in-plane permeabilities, are considered in a homogenized approach to the GDL region [1, 2, 3]. The comprehensive review of Ozden et al. [4] addresses this and other material characteristics of GDLs.

The permeability of the porous material was obtained by several researchers using Lattice Boltzmann (LB) simulations, utilizing different materials and under varying conditions. Deshpande et al. [5] investigated the permeability of a system of parallel fibers using 2D LB simulations, observing numerical variations in the absolute values of the calculated permeability caused by lattice and geometry characteristics. LB simulations in 3D were applied by van Doormaal and Pharoah [6], as well as by Nabovati et al. [7], to determine the permeability of fiber-based GDLs. They investigated the through-plane and in-plane permeabilities of various arrangements of straight fibers. Book and Venturoli [8], in turn, evaluated the consistency of their LB simulations according to the permeability applied to Berea sandstone for several porosities and sample sizes. They observed variation in the absolute values of the calculated permeability. The trend in this LB simulation is in a good agreement with systematic relationships in varying conditions. However, large variations in the absolute values of the permeability were observed, although the permeability was in the same order of magnitude as experimental or literature values.

Koponen et al. [9] already simulated creeping flow through woven material in the past century, finding a systematic relationship with the porosity of the material as proposed by the Kozeny-Carman equation. The same group also proposed different approaches for calculating tortuosity from the velocity field of a transport simulation [10]. The tortuosity can be calculated by integrating the streamlines in the porous structure. Simplifications led to proper relationships with the porosity of the material, but decreasing accuracy according to the level of simplification. One of the approaches can be applied without calculating the streamlines. The different methods of tortuosity calculations were compared by

Duda et al. [11], who showed the applicability of the simple approach under the assumption of incompressible fluids and non-reentrant flows. Differences between the geometrical and flow-based tortuosity were discussed by Guo [12]. The general accuracy of LB simulations, with a focus on the algorithm itself, was analyzed by Gray and Boek [13]. Berg [14], correspondingly, analyzed the calculation of flow characteristics from streamlines from a mathematical viewpoint.

The limitation of the accuracy of LB simulations on coarse grids, as they often occur on reconstructed geometries with structures in the micrometer size, has been investigated by several groups. For instance, Thomas et al. [15] studied the numerical error in the calculation of permeability depending on the resolution of the underlying lattice. Khirevich et al. [16] pointed out the limited accuracy of LB simulations on coarse grids (which are often available from the reconstruction of the underlying material). Gao et al. [17] analyzed the impact of the sample size on transport properties obtained from transport simulations.

Espinoza et al. [18] studied the material properties of regular porous structures, as well as in GDL structures created by a stochastic model [19] using LB simulations. Paper-type GDLs were reconstructed using a stochastic model and featuring the distribution of the orientation of the fibers by Simaafrookhteh et al. [20]. They calculated the properties of the porous structure from throughplane and in-plane transport simulations. Anisotropic permeability values were also observed in three coordinate directions. The impact of compression on carbon cloth was investigated by Rama et al. [21] using LB simulations. Gao et al. [22] analyzed permeability in compressed and uncompressed carbon cloth GDLs. meanwhile, our own group investigated the impact of compression on paper-type [23, 24] and non-woven GDLs [25] through the use of LB simulations in reconstructed material, and also in the realizations of artificial geometries that are stochastically equivalent to the real material. Didari et al. [26] used a genetic algorithm to model the curved fibers of GDLs, validating their model against the Freudenberg GDL. A comprehensive review of LB simulations of PEFCs – including the characterization of GDLs – was presented by Molaeimanesh et al. [27]. Salomov et al. [28] used LB simulations to calculate the permeability of woven GDLs. The in-plane characteristics of several GDL types, including the Freudenberg, were determined by Rashapov and Gostick [29].

The influence of compressive stress on the morphology of the micro structure of different kinds of GDLs – one of them the Freudenberg H2315 C2 – was analyzed by Atkinson et al. [30]. Ozden et al. [4], in turn, presented a comprehensive overview of the characteristics of GDLs from different manufacturers, only reporting on the measured in-plane permeability of GDLs for rare cases.

An experimental determination of GDL permeability is most often based on a measurement of the pressure drop formed by a flowing medium through a porous material, where the permeability is then evaluated by means of Darcy's Law [31, 32, 33, 34, 35, 36, 37, 38]. The Forchheimer effect was considered in works where fluid flow velocity exceeded the conditions of creeping flow [32, 34, 39, 40]. Through-plane permeability is mostly evaluated for uncompressed sample [32, 33, 34, 41, 42] because the fluid flow occurs in the same direction in which the compression is applied. Even though such a setup is technically more complicated, some studies [35, 36] presented the results of through-plane permeability for different compressions. On the contrary, in the case of in-plane permeability, the measurements for a different degree of GDL compression are more frequent [31, 32, 35, 37, 38, 43, 44]. Unfortunately, data for uncompressed GDL permeability are rare, but as an example, data for the highest porosity, published by Gostick et al. [32], are close to this case.

The through-plane permeability of the GDL is strongly reduced by the presence of micro-porous layer (MPL) [33, 34]. Williams et al. [33] characterized different types of GDLs and found an order of magnitude difference between bare paper (8.7 - 31 μm²) and paper or cloth with MPL (0.07 - 1.85 μm²). The same trend was observed by Orogbemi et al. [34] – through-plane permeability of bare paper (18 μm²) declined below 1 μm² for the carbon loading of an MPL of 2.5 mg cm⁻². The presence of a binder (polytetrafluorethylene, PTFE) also leads to a decrease in through-plane permeability [41, 39, 42]. Prasanna et al. [41] measured the values of the through-plane permeability of carbon paper,

which declined from 10.6 to 5.3 µm², with the PTFE content increasing from 10% to 40%. An analysis of the influence of PTFE content was also conducted my Gurau et al. [39], who evaluated the permeability of bare macroporous substrate (single-sided carbon fiber cloth from E-Tek) to 13 µm². The content of the PTFE led to a decrease in through-plane permeability by an order of magnitude. Gostick et al. [32] studied different paper-type GDLs, both with and without the content of PTFE, and observed values in a range from 5.7 to 37.4 µm², but due to the different materials used it is hard to evaluate trend with respect to PTFE content. Mangal et al. [42], in addition to analyzing PTFE content, studied the influence of a number of layers in the range from 1 to 4 used for the experiment and did not find a notable impact of this parameter on the measurements' accuracy. The through-plane permeability of a GDL at one value of compression was presented by Hussaini and Wang [36] for Toray papers and E-Tek GDL. They obtained values in the same order of magnitude as presented in the literature. Finally, Becker et al. [35] studied the impact of compression level on the value of through-plane permeability. They observed its decrease with increasing compression levels; however, this was less significant compared to in-plane permeability.

The apparatus for measurement of in-plane permeability are more difficult regarding the definition of a cross-section area of fluid flow. Generally, there are two different set-ups: (i) cylindrical flow-through cell with radial flow direction [31, 37, 38, 39] or (ii) a cell with a straight flow in a single direction [32, 36, 44]. The former is less demanding on sealing, but the possible information about anisotropy is lost. On the contrary, the latter configuration allows the study of GDL anisotropy, but a satisfactory degree of sealing is challenging to achieve.

Feser et al. [31] used a radial flow permeability testing apparatus to investigate three types of GDLs: the non-woven type (SGL 31 BA); cloth (AvCarb 1071-HCB); and carbon paper (TGP-60H), at different degrees of compression. All of the types showed decreasing in-plane permeability with increasing compression. This dependence was most pronounced for the non-woven-type GDL, which decreased from 43 μ m² for a compression of 13%, to 2.2 μ m² for a com-

pression of 24%. The lowest decrease in in-plane permeability was exhibited by carbon paper-type GDL. In the range of compression from 4% to 24%, the in-plane permeability values only dropped from 11 µm² to 5 µm². Nitta et al. [37] evaluated the in-plane permeability of carbon paper SGL Sigracet 10-BA. The reduction in the permeability was as much as one order of magnitude at compression by 35% (from 27 µm² to less than 1 µm²). A very similar apparatus to that of Nitta et al. [37] was used by Zhiani et al. [38]. They studied the properties of Toray paper TGP-H060ST with an MPL prepared in four different ways. The in-plane permeability of the most permeable sample declined from 4.46 to $0.39 \,\mu\text{m}^2$ as the compression ratio grew from 5.5% to 21%. Becker et al. [35] measured both the through-plane and in-plane permeability a a function of compression. They observed that the values of in-plane permeability are higher than the through-plane variety across the entire range of compression under consideration. As is mentioned above, the in-plane permeability was shown to be more sensitive to the degree of compression, as the through-plane permeability decreased from 5 to 2 µm², whereas the in-plane version dropped from 24 to 4 µm². In other works [32, 36, 39], it has also been found that the value of in-plane permeability is mostly higher than its through-plane counterpart. Anisotropy in a different in-plane direction is presented by Gostick et al. [32], who employed the flow-through cell with a straight flow in a single direction and found an anisotropy for SGL Sigracet 10BA and AvCarb P75 (ratio between permeability for two perpendicular directions $\kappa_A/\kappa_B > 1.6$). Sample SGLs Sigracet 24BA ($\kappa_A/\kappa_B=0.93$) and 34BA ($\kappa_A/\kappa_B=1.38$) showed only a moderate tendency toward anisotropic behavior. Furthermore, Banerjee and Kandlikar [43] showed that the in-plane permeability of carbon papers/non-woven GDLs was compressed by approximately 15% and increased with rising temperature in the range from 20 to 80 $^{\circ}$ C.

The values of permeabilities in the literature range from hundredths to tens of μm^2 depending on a material type and its treatment. To the best of our knowledge, an experimental study of Freudenberg GDL has not yet been conducted.

Cihan et al. [45] compared permeability in fractal porous media calculated from LB simulations with two models that analyze two-dimensional slices of the material. They analyzed random sponge material with Reynolds numbers in the range of 0.4. The relevance of material properties like permeability and tortuosity is represented by applications in several fields using different methods. The permeability of GDLs was related to properties of the micro structure by Tamayol et al. [46] and Hooman et al. [47]. Beyhaghi and Pillai [48] calculated tortuosity from streamlines obtained from Finite Elements Method (FEM) simulations. Anisotropic permeabilities require the application of Darcy's law in its generalized form. This was performed by Degan et al. [49], who analyzed convection in porous media. Magnico [50], in turn, investigated isotropic and anisotropic metallic foams. More complex scenarios were analyzed by Zijl [51] using analytic methods, and by Lang et al. [52] with numerical investigations.

One of the challenges in experimental validation of transport simulation in porous material is the different size of the samples for measurements and of the simulation domain. Typically, samples for measurements have a size in the cm range to obtain macroscopic properties that are relevant for real applications. On the other hand, simulation domains often have sizes in the mm or µm range. Especially in presence of superposed structures [25], the size of the representative elementary volume (REV) [53] can be as large as the smallest relevant structures in the application, e.g., gas channels. The size mismatch can be overcome by creating series of geometries that are stochastic equivalent to the real structure, and then run series of simulations on these artificial 3D structures.

In our previous studies [25], hydrogen transport was simulated in a small section of H2315 GDL from Freudenberg. Anisotropic transport properties were then investigated in real micro structures, as well as in realizations of a stochastic model representing the micro structure.

In this work, the properties of permeability and tortuosity were analyzed in three flow directions. Previous studies [25] have shown a systematic anisotropy of the in-plane properties – permeability and tortuosity – but there was a deviation between the absolute values of the permeability in the real and stochas-

tic materials. The permeability of Freudenberg H2315 GDL was measured in through-plane and in-plane scenarios. In the in-plane setup, the GDL was inserted in two orientations in order to analyze in-plane anisotropy. Transport simulations were then applied with slightly changed boundary conditions compared to previous works.

2. Experimental set-up

The experimental evaluations of in-plane and through-plane permeability were performed for the GDL of H2315, Freudenberg. This GDL does not contain a micro-porous layer and does not have any hydrophobic treatment. This type of GDL was chosen to determine the properties of the GDL substrate itself. Any treatment of the GDL can influence the transport parameters of the material.

The experimental measurements provide us with a dependence of pressure drop on a flow rate formed during a gas flow through a sample of the GDL. The overall permeability κ in the direction of the flow was then evaluated using Darcy's law that is valid for viscous gas flow in porous media [53]; see Eq. (1):

$$\Delta p = \frac{\overline{v}\mu L}{\kappa} \tag{1}$$

Here, Δp represents the measured pressure drop, \overline{v} is the mean value of the gas flow velocity calculated from the measured volumetric flow rate and flow cross-sectional area (without GDL) and μ stands for the dynamic viscosity of the particular gas. The symbol L represents the length through which the gas had to pass in the GDL.

The permeability value was determined for hydrogen (anode side of the fuel cell) and nitrogen (simulating air on the cathode side of the cell). All of the experiments were performed at an ambient temperature of around 23 °C. The outlet of an experimental cell was open to the atmosphere.

Prior to the permeability measurements, the porosity of the studied GDL

was experimentally determined by using equation 2:

$$\varepsilon_{\rm GDL} = 1 - \frac{\rho_{\rm A}}{\rho_{\rm S}}$$
 (2)

Here, $\rho_{\rm S}=1.77~{\rm g~cm^{-3}}$ represents a skeletal density of the solid phase of the GDL determined by means of the Helium pycnometry. An apparent density $\rho_{\rm A}$ of the GDL was obtained from the measured GDL thickness of $w_{\rm GDL}=192~{\rm \mu m}$ and the GDL loading of $m_{\rm GDL}=94~{\rm g~m^{-2}}$, $\rho_{\rm A}=m_{\rm GDL}/w_{\rm GDL}=0.49~{\rm g~cm^{-3}}$. The resulting porosity of the GDL is $\varepsilon_{GDL}=0.73$. This is in good quantitative agreement with the calculated porosity of the original GDL geometry (O – from BESSY synchrotron); see section 5.

2.1. Through-plane permeability

The experimental cell for measurement of the through-plane permeability is depicted in Fig. 1. The sample has a circular shape with a diameter of 15 mm. The single GDL does not have a pressure drop that could be reliably measured. Due to this, several layers of the GDL sample were placed in the experimental cell. The number of GDLs used is changed to eliminate the influence of the inhomogeneity of the material, but it is limited by the experimental set-up. In the present case, the limiting factor is the range of the manometer, which is able to measure the pressure drop up to 500 Pa. In addition to the GDLs, two plastic meshes and expanded metal meshes are placed below the GDLs as a mechanical support. Firstly, a set of measurements without GDLs was performed to set the correction of the experimental set-up. Subsequently, the dependence of the pressure drop on the gas flow rate was measured for the cell with the required number of GDL layers. The space above the GDL sample was sufficient to provide a uniform gas supply to the top GDL layer.

2.2. In-plane permeability

The GDL in-plane permeability was determined using a flow-through cell, as shown in Fig. 2. The cell comprised two parts: the first was the bottom part with the inlet and outlet chambers and ports for the manometer connection. The

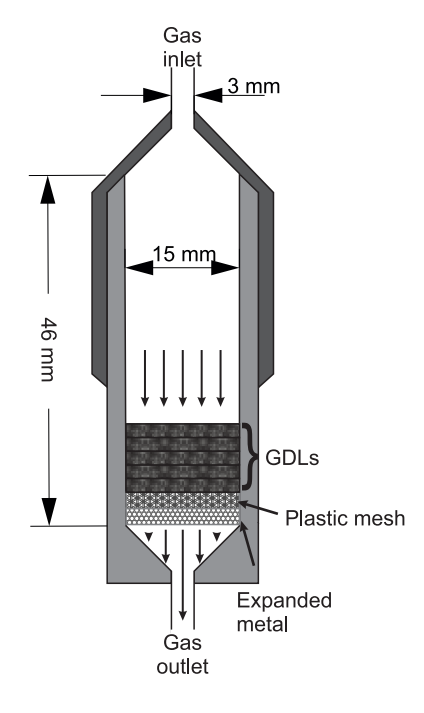


Fig. 1. Experimental set-up for the measurement of the GDL's through-plane permeability.

second was a lid with a slot for the GDL sample. The depth of the slot defined the thickness of the GDL sample. Three lids with different slot thicknesses of 125, 159 and 168 μ m, respectively, were analyzed. As the uncompressed GDL H2315 had a thickness of 192 μ m, the measured compressions were 13%, 17% and 35%, respectively. The size of the sample was $50 \times 40 \text{ mm}^2$. The in-plane permeability can show anisotropy in permeability depending on the orientation of the GDL sample. Due to this, the measurements were also performed for a GDL rotated by 90°.

3. Simulation setup

The material properties – permeability and tortuosity – were calculated from transport simulations in the micro structure of the Freudenberg H2315 GDL and also in representations of a stochastic model describing the micro structure.

The real structure of the material was obtained from the BESSY synchrotron

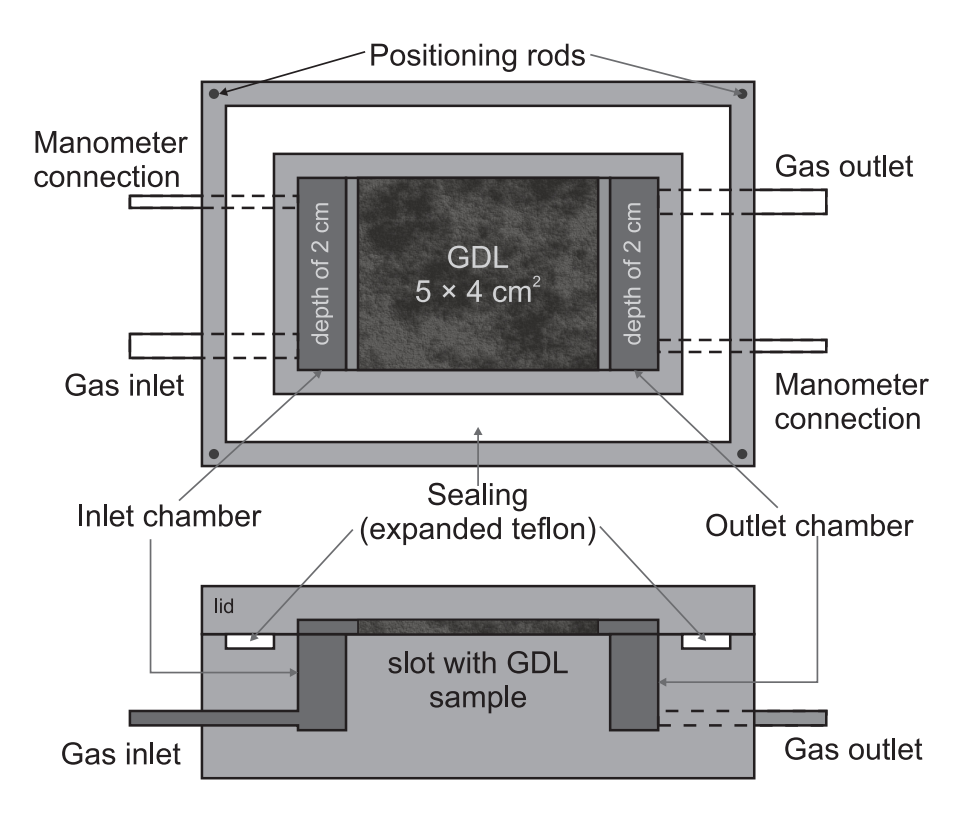


Fig. 2. Experimental set-up for measurement of GDL in-plane permeability. The top- and side-view (thickness of the slot with the GDL is not to scale).

at the Helmholtz Center in Berlin. Gaiselmann et al. [54, 55] developed a mathematical model that is able to create realizations that are stochastically equivalent to the real micro structure of the material. Both the real structure and depictions of the stochastic model are represented as a series of images that build a section of a GDL layer. Fig. 3 (A) depicts how the image series define a three-dimensional frame for transport simulations. Upstream and downstream free space is added to allow the specification of meaningful inlet and outlet conditions.

The through-plane flow direction was marked by the x coordinate in Fig. 3 (A), and therefore the images represent the in-plane directions are along the (y, z) coordinates. Fig. 3 (B-E) shows sample images from which the micro structure for the transport simulation was built. Fig. 3 (B) shows several orientations

of fiber bundles, some of them marked with red lines. One of these – also shown in Fig. 3 (C) – seems to appear systematically. Tötzke et al. [56] and Gaiselmann et al. [55] argue that water entangling during the manufacturing process leads to parallel structures of local gaps in the GDL. They are parallel to the edges of the delivered sheets and are visible to the naked eye. The orientations of the samples in the in-plane experiments mentioned in section 2.2 are oriented in the following manner:

- A: Flow of gas media occurs parallel to these structures.
- B: Flow of gas media occurs perpendicular to these structures.

In particular, Tötzke et al. [57] identified a distance of 500 µm between parallel fiber bundles. Fig. 3 (C) shows one layer of the real geometry, consisting of 230 images. Fiber bundles can be identified in a certain angle related to the coordinate axes. Fig. 3 (C) shows the orientation of the fiber bundles in the real geometry of layer 130 marked by a red line. The red line was drawn manually in the image to mark the fiber bundles, while the tool gimp [58] helped to measure an angle of 24.5° between the fiber bundles and y axis. Fig. 3 (D) illustrates the rotation of the simulation coordinates (y, z) to the coordinates (a, b) rotated counterclockwise by an angle α . In Fig. 3 (E), a layer of one of the stochastic geometries is rotated by -24.5° , aligning the simulated y coordinate in the direction of the fiber bundles (red line in Fig. 3 (C)) of the real geometry.

The stochastic geometry model of Gaiselmann et al. [55] considers the concept of fiber bundles in one dominating direction. As is shown in Fig. 3 (E), they are oriented along the y coordinate. The stochastic models are represented by 240 images in the uncompressed case. Simulations were then performed with different kinds of geometries.

- (O) Original geometry obtained from the BESSY synchrotron. 230 images of size 1500 by 1500 represent a GDL section of 1.25 by 1.25 mm².
- (A-F) Six representations of the geometry model, which are the stochastic equivalent of the real data were taken, all of them uncompressed and with 30%

compression.

(F) One of the realizations is also available with a 10% and 20% compression.

As already described in detail in our previous work [25], the transport of gases was simulated using the BGK scheme of the Lattice Boltzmann method. The D3Q19 discretization implemented in the Palabos software [59] was used as a basis for the transport simulations in the GDLs.

Inlet conditions were specified with constant gas velocity. The value was calculated by Faraday's law according to the gases to be converted at a current density of 1 A cm⁻² and an operating temperature of 25 °C – also known as a Dirichlet boundary condition. The flow of hydrogen converted at 1 A cm⁻² leads to creeping flow conditions with Reynolds numbers below 10^{-3} [25]. At the outlet, a constant pressure was applied, which is a Neumann condition on the velocity. At the side boundaries – y and z direction in the case of through-plane simulations – slip conditions were applied to the walls.

For in-plane transport simulations, the transport is simulated in a similar simulation frame as is shown in Fig. 3 (A), but with free space and inlet/outlet conditions defined at the borders in y or z directions, depending on the flow orientation.

3.1. Differences to previous studies

Transport simulations on the H2315 GDL and its stochastic representations have already been presented in the literature [25]. In comparison to the earlier results, two conditions were modified.

- 1. The simulations by Froning et al. [25] were run with hydrogen at an operating temperature of 160 $^{\circ}$ C.
- 2. The conditions at the side boundaries slip conditions are different from our previous studies [25], where no-slip boundaries were specified. Slip conditions might be more precise, especially in the in-plane directions where large areas and small GDL thicknesses are affected by the boundary conditions.

4. Results of the experimental part

The dependence of pressure drops on the mean gas flow velocity is linear within the range of experimental conditions under investigation. Hydrogen shows lower pressure drops compared to nitrogen due to its lower dynamic viscosity. The slope of each line was determined by means of the least squares method.

4.1. Through-plane permeability

Measurements for the evaluation of through-plane permeability were performed for different number of layers (from 7 to 15) GDLs. The results are summarized in Table 1 and Fig. 4 (A). Each measurement provides a value of through-plane permeability. It can be seen that the data show dispersion, which will be discussed in the next paragraph.

The resulting average permeability of the GDL is $(8.6 \pm 0.5)~\mu\text{m}^2$. The deviation can be explained by inhomogeneity in the GDL material and/or by a bypass gas flow along the wall of the cell. Inhomogeneity in the GDL can arise during production of the GDL. The bypass flow can appear due to the potential existence of small gaps between the cell wall and perimeter of the GDL sample. The gaps for the bypass flow can be formed by: (a) a certain difference in the folding of the individual GDLs into a non-ideal pillar; and (b) the mechanical defects at the edge of the sample formed by cutting the samples of the required diameter.

Fig. 4 and Table 1 show that there is no big difference between the permeability for hydrogen and nitrogen. This confirms Darcy's law (Eq. (1)) that considers the permeability κ as being independent from the gas itself.

4.2. In-plane permeability

Here, the impact of the GDL compression was evaluated. This is shown by the fact that in the fuel cell, reacting gasses must pass through the GDL of different degrees of compression (below the channel vs. below the rib). It is probable that the anisotropy is hidden by the experimental error inherited

Table 1. Summary of the results for measuring of the through-plane measurements.

Gas	Number of GDLs	Through-plane permeability			
		$/~\mu\mathrm{m}^2$			
N_2	7	8.47			
	10	8.45			
	10	8.17			
	10	9.19			
	10	9.15			
	10	8.63			
	12	8.51			
	15	9.08			
H_2	7	9.08			
	10	8.14			
	10	9.19			
	10	8.20			
	10	8.12			
	12	9.12			
	15	7.82			

to the method. The results of the experimental determination of the in-plane permeability of the GDL at different orientations and degrees of compression are summarized in Table 2 and Fig. 4 (B). The in-plane permeability decreases with increasing compression. The decrease is not linear. The highest compression (35 %) leads to damage to the GDL sample, and so this value is affected with a larger experimental error.

Anisotropy for different orientations (A and B) of the GDL sample was not proven by this method. The difference between the measured in-plane permeabilities in the two directions is slightly larger than the experimental uncertainty - the ratio κ_B/κ_A is 1.05 for 13 % compression and 1.06 for 17 % compression.

For the 35 % compression, the ratio κ_B/κ_A is 1/1.06 is the reciprocal value. But in this case the experimental error is larger because of the damage of the GDL sample.

Table 2. Summary of results for the measuring of in-plane measurements.

Orientation	Compression	In-plane permeability		
	/ %	$/~\mu\mathrm{m}^2$		
A	13	$2.7~\pm~0.2$		
В	13	$2.84~\pm~0.08$		
A	17	$2.08~\pm~0.05$		
В	17	$2.2~\pm~0.1$		
A	35	$1.9~\pm~0.3$		
В	35	$1.8~\pm~0.2$		

5. Simulation results

Transport simulations were run in real micro structures of H2315 and in six representations of a geometry model, which is stochastically equivalent to the real micro structure of the material according to Gaiselmann et al. [54]. The simulations were performed with hydrogen at 25 °C.

Fig. 5 shows stream tracers in the central region of the transport simulations in the uncompressed stochastic geometry D. All simulations were applied to a set of 240 images of 1500 by 1500 in size, representing a section of 1.25 mm by 1.25 mm of a GDL with 200 µm thickness (geometries A-F, uncompressed). For the visualization of the stream tracers, only the central region was chosen – 1100 by 1100 for the through-plane simulation and 900 by 1500 for the inplane simulations. The effective properties – permeability and tortuosity – were calculated from the simulated velocity field. The full results are summarized in Table 3, including the transformation introduced in section 5.2.

5.1. Through-plane simulations

For geometry O – the reconstruction of the real micro structure – a higher number of GDLs for the through-plane simulation were emulated by repeating the stack of images. For two GDLs, the through-plane permeability was calculated in this way as 6.47 μ m² and 6.42 μ m² for three GDLs. This is close to the single GDL value of 6.24 μ m² reported in Table 3. For this reason, the through-plane simulations for the other cases were only run in single GDL domains.

Simulations under different conditions – 160 °C, as used by Froning et al. [25] – and for nitrogen, which was also used in the experiments, led to identical results. The change in the boundary conditions – slip conditions instead of wall (no slip) boundary conditions – led to a slight change in the absolute value of the permeability. Therefore, the values in Table 3 differ from the corresponding table in our previous study [25]. The through-plane permeability of geometries A-F ranges from 9.35 μ m² to 10.18 μ m² in Table 3 for 0% compression – in Froning et al. [25], it was 9.95 μ m² to 10.85 μ m². For a 30% compression, the range of 4.05 μ m² to 4.70 μ m² changed to 4.59 μ m² to 5.09 μ m² in accordance with the boundary condition. However, the qualitative trend is the same: the in-plane permeability is larger than the through-plane permeability, and also the anisotropy in the two in-plane directions was observed in the simulations of both types of boundary conditions.

Fig. 6 shows the layer-wise porosity of geometry O. The images are ordered in the through-plane flow direction (x coordinate). The average porosity is 77%, but the layer-wise values are slightly larger for the first set of images and significantly larger at the end of the scale. This is represented by fewer fibers in this region. The porosity profile presented in Fig. 6 qualitatively matches the porosity profiles observed on paper-type GDLs by Fishman and Bazylak [60], and Niu et al. [61]. The spatial inhomogeneity is not caused by any additives like binder, MPL, or others because H2315 is a base material of Freudenberg. A porosity profile as shown in Fig. 6 can cause inhomogeneous morphological changes in the micro structure under compression because the outer regions of

the GDL are less robust than the inner ones. Therefore, it is expected that the porosity profile becomes more homogeneous under compression. In this case, the Kozeny-Carman equation is not valid. A homogeneous morphological change of the micro structure is also the basis of the compressed geometry model (geometries A-F of the simulations). The average porosity of geometry O was 76.5%, but the clearly relevant region shown in Fig. 6 is lower. For the inner region – omitting 40 image layers from each side – the porosity was 75.1%. The artificial geometries A-F were constructed under the assumption of a uniform porosity – but with statistical variations. The porosity of geometry F was:

- 1. 76.5% for 0% compression;
- 2.74.0% for 10% compression;
- 3.70.9% for 20% compression;
- 4.67.0% for 30% compression.

For any pragmatic handling of the non-woven GDL, the outer regions could be smoothly compressed. In this case, the local porosity of the outer regions decreases, even if no compression is intended – possibly until an almost homogeneous local porosity profile is reached. In this sense, the 10% compression of geometry F is closest to the inner region of the local porosity of geometry O, without the 40 side image layers. Given a mechanical force in the GDL, it was assumed that regions of high porosity (few fibers) were deformed more than regions of low porosity (many fibers). This justifies the comparison of the 10% compressed geometry F with the through-plane experimental results, neglecting the inhomogeneous deformation at the beginning of the process. The simulated permeability of 8.99 μm^2 fit well to the through-plane experiments $(8.6 \pm 0.5 \ \mu m^2)$.

5.2. In-plane simulations

Because the stochastic geometry model creates its fiber bundles along the coordinates their orientation is skewed to the manufacturing direction, as illustrated in Fig. 3 (C-E). The z-direction is the in-plane direction that is normal to

the fiber bundles. Applied to the transport simulations on stochastic geometries A-F, Darcy's law from Eq. (1) must be applied in its vector form:

$$\mu \vec{v} = -\bar{K} \nabla P, \quad \bar{K} = \begin{pmatrix} \kappa_y & 0 \\ 0 & \kappa_z \end{pmatrix}$$
 (3)

with \bar{K} being the tensor of permeabilities. For the evaluation of the in-plane characteristics, Eq. (3) is restricted to the two in-plane coordinates y, z (also seen in Fig. 3). According to Degan et al. [49] and Lang et al. [52], a rotation matrix R can be defined as:

$$R = \begin{pmatrix} \cos(\alpha) & -\sin(\alpha) \\ \sin(\alpha) & \cos(\alpha) \end{pmatrix} \tag{4}$$

which rotates the vectors by an angle α . Left side multiplication by R rotates the system in Eq. (3) counterclockwise by angle α :

$$\mu R \cdot \vec{v} = -R \cdot \bar{K} \cdot \nabla P$$

$$= -R \cdot \bar{K} \cdot R^T \cdot R \cdot \nabla P$$

$$\mu (R \cdot \vec{v}) = -(R \cdot \bar{K} \cdot R^T) \cdot (R \cdot \nabla P)$$
(5)

Then, Eq. (5) represents Darcy's law on the rotated system (a,b). In this system, the permeability tensor \bar{K}_{α} can be calculated by Eq. (6):

$$\bar{K}_{\alpha} = R\bar{K}R^{T}$$

$$= \begin{pmatrix} \kappa_{y}\cos^{2}(\alpha) + \kappa_{z}\sin^{2}(\alpha) & (\kappa_{y} - \kappa_{z})\sin(\alpha)\cos(\alpha) \\ (\kappa_{y} - \kappa_{z})\sin(\alpha)\cos(\alpha) & \kappa_{y}\sin^{2}(\alpha) + \kappa_{z}\cos^{2}(\alpha) \end{pmatrix}$$

$$= \begin{pmatrix} \kappa_{y}\cos^{2}(\alpha) + \kappa_{z}\sin^{2}(\alpha) & (\kappa_{y} - \kappa_{z})/2\sin(2\alpha) \\ (\kappa_{y} - \kappa_{z})/2\sin(2\alpha) & \kappa_{y}\sin^{2}(\alpha) + \kappa_{z}\cos^{2}(\alpha) \end{pmatrix}$$
(6)

For measurements in a direction $R \cdot \vec{v} = (\Delta P_a, 0)^T$ in Eq. (5), and $R \cdot \vec{v} = (v_a, 0)^T$. In the b direction $R \cdot \vec{v} = (0, \Delta P_a)^T$ and $R \cdot \vec{v} = (0, v_b)^T$ where indices a and b specify components according to the coordinate system of the

measurements (A, B). According to the one-dimensional Darcy's law (Eq. (1)), the permeabilities κ_a , κ_b can be calculated by Eq. (7):

$$\kappa_a = \kappa_y \cos^2(\alpha) + \kappa_z \sin^2(\alpha)
\kappa_b = \kappa_y \sin^2(\alpha) + \kappa_z \cos^2(\alpha)$$
(7)

For a comparison of the simulated and measured permeabilities, it must be clarified how the coordinates of the simulated and measured systems match each other. The measured permeabilities were obtained from GDLs which that compressed by 13%, 17% and 35%, as is shown in Table 2. For comparison with the simulated in-plane permeabilities, the 10% 20%, and 30% entries of geometry F can be used. The matching of the orientation has two variables: The angle of the fiber bundles was identified as 24.5° in section 3. For the application of Eq. (6), this angle can be positive or negative. Furthermore, the experimental flow direction can be the first or second coordinate in the resulting vectors of this equation. Due to Eq. (7), the absolute values of the permeability do not change with the sign of the angle. Then, the larger value of (κ_a, κ_b) from Table 3 relates to the larger value of the measured in-plane permeabilities. To bring the permeabilities of the transport simulations in the stochastic geometries into agreement with the experiment, the ratio of κ_a and κ_b of the entries for 10%, 20% and 30% compression (case F) in Table 3 should match the ratio of the measured permeabilities in the A and B orientation in Table 2.

The rotation of the simulated permeabilities by 24.5° according to Eq. (7) lowered the ratio of κ_a/κ_b , as is shown in Table 3. However, the in-plane anisotropy – $\kappa_a/\kappa_b = 1.18$ on average – is still larger than the experimental result (1.06) and it is also larger than the corresponding value from the simulations in the reconstructed micro structure (geometry O), where $\kappa_z/\kappa_y = 1.03$. This small ratio can possibly even be caused by a numerical inaccuracy.

An agreement between the measured and simulated in-plane permeabilities was not found for the stochastic geometries. In representations A-F of the stochastic geometry model, the simulated permeabilities, as well as the amount of in-plane anisotropy, appear to be overestimated. One reason for this can be the fact that fiber bundles were found in different directions in Fig. 3 (B). Although a superstructure caused by water entangling can be identified, it does not seem to dominate the in-plane gas flow. On the other hand, the discussion above shows that an impact of the dominating orientation of the fiber bundles cannot be completely dissolved by rotating the material. As a logical consequence, the other fiber bundles, observed in several in-plane directions in the images, seem to weaken the influence of fiber bundles caused by water entangling. It is possible that there are additional manufacturing parameters, leading to the other fiber bundles.

The inhomogeneous porosity illustrated in Fig. 6 is caused by fewer fibers in the outer regions of the GDL. For in-plane transport simulations, this leads to a small amount of bypass flow which, in consequence, smooths the anisotropy in the center region of the GDL.

The bypass flow is depicteded in Fig. 7 (A) and (B). The simulation was performed on a micro structure specified on a lattice of $1500 \times 230 \times 1500$. The flow lines are visualized in a 1500 \times 230 \times 870 section in order to keep the Visualization ToolKit (VTK) file small. The in-plane flow in the micro structure of geometry O shows areas of higher velocity in the outer regions of the GDL. This is visualized by flow lines in dark red in Fig. 7 (A), and also by a concentration of red-colored areas at the top and bottom regions in the slices of the velocity distribution presented in Fig. 7 (B). The higher velocity is preferably observed in regions of lower local porosity as per the profile displayed in Fig. 6. This inhomogeneity leads to a higher mass flow at the top and bottom of the GDL. Therefore, the calculation of a permeability according to Eq. (1) does not specify a material property, because Darcy's law takes a volume average, assuming homogeneous flow characteristics in the micro structure. For comparison, the in-plane velocity distribution of an artificial geometry (F) is shown in Fig. 7 (C) and (D). This geometry was chosen in its 10% compressed variant because of the through-plane discussion above. Although the absolute permeability values differ from the measured ones (Table 2) and also from the simulations in geometry O (Table 3), the velocity profiles can be qualitatively analyzed. Due to the underlying stochastic model [55], the porosity profile is more homogeneous than the profile of geometry O. In Fig. 7, the red areas of the flow lines (C) and the velocity distribution (D) still show a variation, but the extreme values are more homogeneously distributed across the volume of the GDL than before.

Due to the bypass effect in the in-plane simulations, the inner region of geometry O was extracted for another in-plane simulation on a more homogeneous micro structure. The inner region was selected by omitting 40 images from the top and bottom regions of this geometry according to the porosity profile in Fig. 6. Because only 150 images were left to define the micro structure, the remaining geometry was copied and stacked upon itself. The result is a micro structure based on 300 images. It is more important to avoid undesirable wall effects in case of an extremely thin GDL layer than to have a drawback of an unrealistic identical copy of two half-layers. Therefore, the in-plane gas flow was simulated in a micromstructure defined by two identical sets of 150, to total 300 images.

The simulations led to an average permeability of 6.56 μ m² and a tortuosity of 1.163, as shown in Table 4. The permeabilities in two perpendicular in-plane directions do not indicate an anisotropy in the two in-plane directions. The compression is marked as 0++ in the table to illustrate that the micro structure was obtained from an uncompressed reconstruction of the real material. Because the inner core of the inhomogeneous micro structure was selected, this region possibly represents a slightly compressed material with an unknown compression rate. The new permeability values are closer to the measurements, but it is also smaller than the old value from Table 3. The apparent discrepancy of having a smaller permeability in a micro structure represents a higher compression and is caused by the porosity profile. The original data, with its inhomogeneous porosity caused a bypass flow in the in-plane 1 (y-) direction, as shown in Fig. 7 (A). For the new simulations, the porosity is almost homogeneous. The resulting in-plane gas flow is shown in Fig. 8. While the simulations were performed on a

lattice of $1500 \times 300 \times 1500$, the flow lines are visualized in a smaller section of $1500 \times 300 \times 730$ in order to keep the VTK file small. The slice in front of the GDL shows the y component of the velocity and also a red frame identifying the visualization region of Fig. 7 (A) and (B). Another two red lines in this frame show the kernel region of the GDL with the homogeneous porosity profile according to Fig. 6. With these reference lines, the dark blue shadows of the fibers can be identified on the front slice and the stacked copy of the micro structure is represented by identical shadows in front of the GDL. In the right section, a large red region can be identified that is also shown twice, with the white numbers 1 and 2 in Fig. 8. On the other hand, the location numbers 3 on the top border and 4 on the bottom border are obviously influenced by the wall – the red color in these locations is darker than their counterparts at the centerline where the micro structure is copied.

Compared to the visualization in Fig. 7 (A), the colors of the flow lines show a more homogeneous flow field. This is also a precondition of Darcy's law (Eq. (1)), which is used for the calculation of the permeability from the simulated flow field. Therefore, the in-plane simulations on the kernel micro structure are more reliable than the in-plane values shown in Table 3. However, the compression level is potentially an unknown but sensitive parameter that can cause deviations.

The bypass flow can be relevant, especially for in-plane gas transport in thin layers. The contact of the wall to the rough GDL surface can have a large impact on the flow distribution in the porous micro structure. However, for fuel cell applications using GDL material with MPLs, the situation may change, as already noted by Atkinson et al. [30].

6. Conclusion

The through-plane and in-plane permeability of Freudenberg H2315 was experimentally determined. The through-plane permeability is slightly higher, but it is on the same order of magnitude as the in-plane permeability. This corresponds to the arrangement of the carbon fibers in GDL having shorter contact with streaming gas during the experiment. Anisotropy for two perpendicular directions of in-plane permeability was not proven. It can still be observed, but the extreme values of the simulations and the normality of the bundles were not measured. The orientation of the fiber bundles in the manufactured material include not only the clearly visible parallel structures caused by water entangling, but also other pieces of bundled fibers in different directions.

The trend for the in-plane permeability is similar in the measured and simulated data. For the uncompressed case, the values are also in quantitative agreement. The relationship of the through-plane vs. in-plane permeability in the simulations is inverse to the measured data – despite the fact that the in-plane permeability was measured for different compression rates than the through-plane permeability. The simulated through-plane permeability was smaller than the in-plane values. The in-plane simulations showed a high sensitivity to inhomogeneities in the micro structure because of the formation of the bypass flow. Further experimental and simulation investigations could help to illuminate the relationship of the through-plane and in-plane characteristics of GDLs.

Acknowledgements

The experimental work was supported by the European Regional Development Fund – Project 'Fuel Cells with Low Platinum Content' [grant number CZ.02.1.01/0.0/0.0/16_025/0007414]. Simulations were performed using the hardware of the Jülich Supercomputing Centre [grant number CJIEK30]. The authors thank Christopher Wood for proofreading the manuscript.

References

[1] M. Kvesić, U. Reimer, D. Froning, L. Lüke, W. Lehnert, D. Stolten, 3D modeling of a 200 cm² HT-PEFC short stack, Int. J. Hydrogen Energy 37 (2012) 2430–2439.

- [2] R. Kodým, M. Drakselová, P. Pánek, M. Němeček, D. Šnita, K. Bouzek, Novel approach to mathematical modeling of the complex electrochemical systems with multiple phase interfaces, Electrochim. Acta 179 (2015) 538– 555.
- [3] T. Sousa, M. Mamlouk, K. Scott, A dynamic non-isothermal model of a laboratory intermediate temperature fuel cell using pbi doped phosphoric acid membranes, Int. J. Hydrogen Energy 35 (2010) 12065–12080.
- [4] A. Ozden, S. Shahgaldi, X. Li, F. Hamdullahpur, A review of gas diffusion layers for proton exchange membrane fuel cells—with a focus on characteristics, characterization techniques, materials and designs, Prog. Energy Combust. Sci. 74 (2019) 50–102.
- [5] A. Deshpande, A. Srikanth, N. Praveen, Quantitative estimation of permeability with lattice boltzmann simulations: Representative porous media from composite processing, The Can. J. Chem. Eng. 83 (2005) 808–815.
- [6] M. A. van Doormaal, J. G. Pharoah, Determination of permeability in fibrous porous media using the lattice Boltzmann method with application to PEM fuel cells, Int. J. Numer. Meth. Fluids 59 (2009) 75–89.
- [7] A. Nabovati, E. W. Llewellin, A. C. M. Sousa, A general model for the permeability of fibrous porous media based on fluid flow simulations using the lattice Boltzmann method, Composites Part A 40 (2009) 860–869.
- [8] E. D. Boek, M. Venturoli, Lattice-Boltzmann studies of fluid flow in porous media with realistic rock geometries, Comput. Math. Appl. 59 (2010) 2305– 2314.
- [9] A. Koponen, D. Kandhai, E. Hellen, M. Alava, A. Koekstra, M. Kataja, K. Niskanen, P. Sloot, J. Timonen, Permeability of Three-Dimensional Random Fiber Webs, Phys. Rev. Lett. 80 (1998) 716–719.
- [10] A. Koponen, M. Kataja, J. Timonen, Tortuous flow in porous media, Phys. Rev. E 54 (1996) 406–410.

- [11] A. Duda, Z. Koza, M. Matyka, Hydraulic tortuosity in arbitrary porous media flow, Phys. Rev. E 84 (2011) 036319.
- [12] P. Guo, Lower and upper bounds for hydraulic tortuosity of porous materials, Transp. Porous Media 109 (2015) 659–671.
- [13] F. Gray, E. Boek, Enhancing computational precision for lattice boltzmann schemes in porous media flows, Comput. 4 (2016) 11.
- [14] C. F. Berg, Permeability description by characteristic length, tortuosity, constriction and porosity, Transp. Porous Media 103 (2014) 381–400.
- [15] M. L. R. Thomas, D. B. Ingham, M. Pourkashanian, Prediction of the Permeability of Fibrous Media Using the Lattice Boltzmann Method in Conjunction with Coarse Numerical Lattices, Open Transp. Phenom. J. 2 (2010) 80–89.
- [16] S. Khirevich, I. Ginzburg, U. Tallarek, Coarse- and fine-grid numerical behavior of MRT/TRT lattice-boltzmann schemes in regular and random sphere packings, J. Comput. Phys. 281 (2015) 708–742.
- [17] Y. Gao, Z. Hou, W. X., P. Xu, The impact of sample size on transport properties of carbon-paper and carbon-cloth gdls: Direct simulation using the lattice boltzmann model, Int. J. Heat Mass Transfer 118 (2018) 1325– 1339.
- [18] M. Espinoza, M. Andersson, B. Sundén, Predicting transport parameters in PEFC gas diffusion layers considering micro-architectural variations using the lattice boltzmann method, Int. J. Energy Res. 41 (2016) 565–578.
- [19] M. Espinoza-Andaluz, M. Andersson, B. Sundén, Comparing throughplane diffusibility correlations in PEFC gas diffusion layers using the lattice boltzmann method, Int. J. Hydrogen Energy 42 (2017) 11689–11698.
- [20] S. Simaafrookhteh, M. Shakeri, M. Baniassadi, A. A. Sahraei, Microstructure reconstruction and characterization of the porous GDLs for PEMFC based on fibers orientation distribution, Fuel Cells 18 (2018) 160–172.

- [21] P. Rama, Y. Liu, R. Chen, H. Ostadi, K. Jiang, Y. Gao, X. Zhang, D. Brivio, P. Grassini, A Numerical Study of Structural Change and Anisotropic Permeability in Compressed Carbon Cloth Polymer Electrolyte Fuel Cell Gas Diffusion Layers, Fuel Cells 11 (2011) 274–285.
- [22] Y. Gao, X. Zhang, P. Rama, R. Chen, H. Ostadi, K. Jiang, An Improved MRT Lattice Boltzmann Model for Calculating Anisotropic Permeability of Compressed and Uncompressed Carbon Cloth Gas Diffusion Layers Based on X-Ray Computed Micro-Tomography, J. Fuel Cell Sci. Technol. 9 (2012) 041010-1-10.
- [23] D. Froning, J. Brinkmann, U. Reimer, V. Schmidt, W. Lehnert, D. Stolten, 3D analysis, modeling and simulation of transport processes in compressed fibrous microstructures, using the Lattice Boltzmann method, Electrochim. Acta 110 (2013) 325–334.
- [24] D. Froning, G. Gaiselmann, U. Reimer, J. Brinkmann, V. Schmidt, W. Lehnert, Stochastic Aspects of Mass Transport in Gas Diffusion Layers, Transp. Porous Media 103 (2014) 469–495.
- [25] D. Froning, J. Yu, G. Gaiselmann, U. Reimer, I. Manke, V. Schmidt, W. Lehnert, Impact of compression on gas transport in non-woven gas diffusion layers of high temperature polymer electrolyte fuel cells, J. Power Sources 318 (2016) 26–34.
- [26] S. Didari, Y. Wang, T. A. Harris, Modeling of gas diffusion layers with curved fibers using a genetic algorithm, Int. J. Hydrogen Energy 42 (2017) 23130–23140.
- [27] G. Molaeimanesh, H. S. Googarchin, A. Q. Moqaddam, Lattice Boltzmann simulation of proton exchange membrane fuel cells – A review on opportunities and challenges, Int. J. Hydrogen Energy 41 (2016) 22221–22245.
- [28] U. R. Salomov, E. Chiavazzo, P. Asinari, Pore-scale modeling of fluid flow through gas diffusion and catalyst layers for high temperature proton

- exchange membrane (HT-PEM) fuel cells, Comput. Math. Appl. 67 (2014) $393{\text -}411.$
- [29] R. R. Rashapov, J. T. Gostick, In-plane effective diffusivity in PEMFC gas diffusion layers, Transp. Porous Media 115 (2016) 411–433.
- [30] R. W. Atkinson, Y. Garsany, B. D. Gould, K. E. Swider-Lyons, I. V. Zenyuk, The role of compressive stress on gas diffusion media morphology and fuel cell performance, ACS Appl. Energy Mater. 1 (2018) 191–201.
- [31] J. Feser, A. K. Prasad, S. G. Advani, Experimental characterization of in-plane permeability of gas diffusion layers, J. Power Sources 162 (2006) 1226–1231.
- [32] J. T. Gostick, M. W. Fowler, M. D. Pritzker, M. A. Ioannidis, L. M. Behra, In-plane and through-plane gas permeability of carbon fiber electrode backing layers, J. Power Sources 162 (2006) 228–238.
- [33] M. V. Williams, E. Begg, L. Bonville, H. R. Kunz, J. M. Fenton, Characterization of gas diffusion layers for PEMFC, J. Electrochem. Soc. 151 (2004) A1173–A1180.
- [34] O. M. Orogbemi, D. B. Ingham, M. S. Ismail, K. J. Hughes, L. Ma, M. Pourkashanian, Through-plane gas permeability of gas diffusion layers and microporous layer: Effects of carbon loading and sintering, J. Energy Inst. 91 (2018) 270–278.
- [35] J. Becker, R. Flückiger, M. Reum, F. N. Büchi, F. Marone, M. Stampanoni, Determination of material properties of gas diffusion layers: Experiments and simulations using phase contrast tomographic microscopy, J. Electrochem. Soc. 156 (2009) B1175.
- [36] I. S. Hussaini, C. Y. Wang, Measurement of relative permeability of fuel cell diffusion media, J. Power Sources 195 (2010) 3830–3840.

- [37] I. Nitta, T. Hottinen, O. Himanen, M. Mikkola, Inhomogeneous compression of PEMFC gas diffusion layer, J. Power Sources 171 (2007) 26–36.
- [38] M. Zhiani, S. Kamali, S. Majidi, In-plane gas permeability and thoughtplane resistivity of the gas diffusion layer influenced by homogenization technique and its effect on the proton exchange membrane fuel cell cathode performance, Int. J. Hydrogen Energy 41 (2016) 1112–1119.
- [39] V. Gurau, M. J. Bluemle, E. S. De Castro, Y.-M. Tsou, T. A. Zawodzinski, J. A. Mann, Characterization of transport properties in gas diffusion layers for proton exchange membrane fuel cells, J. Power Sources 165 (2007) 793– 802.
- [40] L. M. Pant, S. K. Mitra, M. Secanell, Absolute permeability and Knudsen diffusivity measurements in PEMFC gas diffusion layers and micro porous layers, J. Power Sources 206 (2012) 153–160.
- [41] M. Prasanna, H. Y. Ha, E. A. Cho, S. A. Hong, I. H. Oh, Influence of cathode gas diffusion media on the performance of the PEMFCs, J. Power Sources 131 (2004) 147–154.
- [42] P. Mangal, L. M. Pant, N. Carrigy, M. Dumontier, V. Zingan, S. Mitra, M. Secanell, Experimental study of mass transport in PEMFCs: Through plane permeability and molecular diffusivity in GDLs, Electrochim. Acta 167 (2015) 160–171.
- [43] R. Banerjee, S. G. Kandlikar, Effect of temperature on the in-plane permeability in the gas diffusion layer of a PEM fuel cell, ECS Trans. 41 (2001) 489–497.
- [44] J. Ihonen, M. Mikkola, G. Lindbergh, Flooding of gas diffusion backing in pefcs, J. Electrochem. Soc. 151 (2004).
- [45] A. Cihan, M. C. Sukop, J. S. Tyner, E. Perfect, H. Huang, Analytical Predictions and Lattice Boltzmann Simulations of Intrinsic Permeability for Mass Fractal Porous Media, Vadose Zone J. 8 (2009) 187–196.

- [46] A. Tamayol, F. McGregor, M. Bahrami, Single phase through-plane permeability of carbon paper gas diffusion layers, J. Power Sources 204 (2012) 94–99.
- [47] K. Hooman, A. Tamayol, M. Dahari, M. Safaei, H. Togun, R. Sadri, A theoretical model to predict gas permeability for slip flow through a porous medium, Appl. Therm. Eng. 70 (2014) 71–76.
- [48] S. Beyhaghi, K. M. Pillai, Estimation of tortuosity and effective diffusivity tensors using closure formulation in a sintered polymer wick during transport of a nondilute, multicomponent liquid mixture, Spec. Top. & Rev. Porous Media 2 (2011) 267282.
- [49] C. Degan, P. Vasseur, N. C. Awanou, Anisotropy effects on non-Darcy natural convection from concentrated heat sources in porous media, Acta Mechanica 179 (2005) 111–124.
- [50] P. Magnico, Analysis of permeability and effective viscosity by cfd on isotropic and anisotropic metallic foams, Chem. Eng. Sci. 64 (2009) 3564– 3575.
- [51] W. Zijl, A direct method for the identification of the permeability field based on flux assimilation by a discrete analog of Darcy's law, Transp. Porous Media 56 (2004) 87–112.
- [52] P. S. Lang, A. Paluszny, R. W. Zimmerman, Permeability tensor of threedimensional fractured porous rock and a comparison to trace map predictions, J. Geophys. Res.: Solid Earth 119 (2014) 6288–6307.
- [53] F. Civan, Porous Media Transport Phenomena, John Wiley & Sons, 2011.
- [54] G. Gaiselmann, R. Thiedmann, I. Manke, W. Lehnert, V. Schmidt, Stochastic 3D modeling of fiber-based materials, Comput. Mater. Sci. 59 (2012) 75–86.

- [55] G. Gaiselmann, D. Froning, C. Tötzke, C. Quick, I. Manke, W. Lehnert, V. Schmidt, Stochastic 3D modeling of non-woven materials with wetproofing agent, Int. J. Hydrogen Energy 38 (2013) 8448–8460.
- [56] C. Tötzke, I. Manke, C. Hartnig, R. Kuhn, H. Riesemeier, J. Banhart, Investigation of Carbon Fiber Gas Diffusion Layers by Means of Synchrotron X-ray Tomography, ECS Trans. 41 (2011) 379–386.
- [57] C. Tötzke, G. Gaiselmann, M. Osenberg, T. Arlt, H. Markötter, A. Hilger, A. Kupsch, B. Müller, V. Schmidt, W. Lehnert, I. Manke, Influence of hydrophobic treatment on the structure of compressed gas diffusion layers, J. Power Sources 324 (2016) 625–636.
- [58] J. M. Ferreyra, GIMP 2.6 cookbook, Packt Publishing, 2011. URL: https://www.packtpub.com/hardware-and-creative/gimp-26-cookbook.
- [59] FlowKit Ltd, Palabos, http://www.palabos.org/, Feb 2, 2018. URL: http://www.palabos.org/.
- [60] Z. Fishman, A. Bazylak, Heterogeneous Through-Plane Distributions of Tortuosity, Effective Diffusivity, and Permeability for PEMFC GDLs, J. Electrochem. Soc. 158 (2011) B247–B252.
- [61] Z. Niu, Z. Bao, J. Wu, Y. Wang, K. Jiao, Two-phase flow in the mixed-wettability gas diffusion layer of proton exchange membrane fuel cells, Appl. Energy 232 (2018) 443–450.

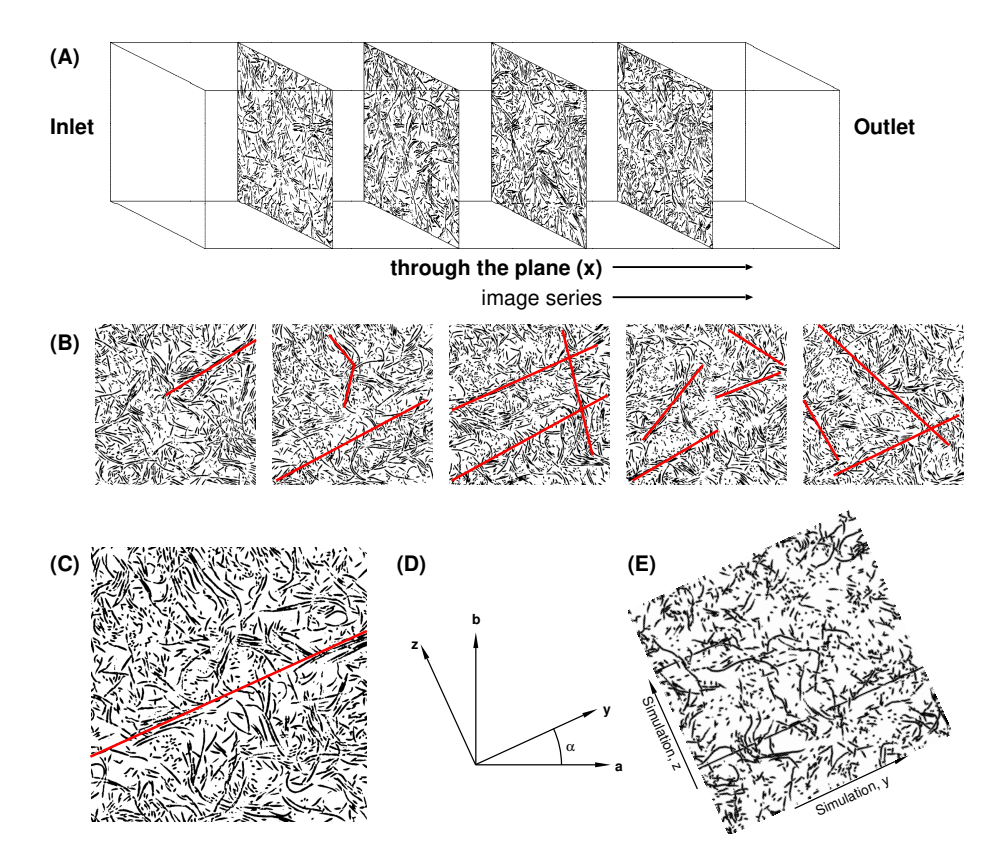


Fig. 3. (A) Simulation frame for image based micro structures. Only four images of the micro structure are shown in the schematic view. The total number ranges from 168 to 240 according to the compression level. (B-E) Orientation of fiber bundles. (B) in layers 50, 82, 105, 124 and 155 of 230 of geometry O. (C) in layer 130 of 230 of geometry O. (D) Sketch of rotation. Simulation system (y, z) is rotated by $-\alpha$ into the measurement system (a, b). (E) Rotated slice of geometry A, layer 172 of 240.

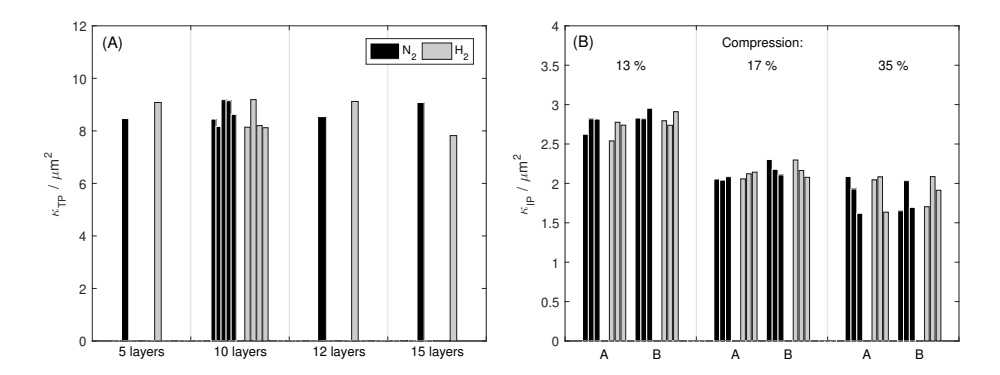


Fig. 4. A: Experimentally-evaluated through-plane permeability for different numbers of layers and for nitrogen and hydrogen; B: experimentally-evaluated in-plane permeability for different degrees of compression, flowing gas and for two perpendicular orientations of the GDL sample, A and B.



Fig. 5. Transport simulations in stochastic geometry D: (A) through-plane simulation, with the flow direction from the bottom to the top; (B) in-plane simulation amongst fiber bundles, flow direction from left to right; (C) in-plane simulation normal to fiber bundles, flow direction from left to right.

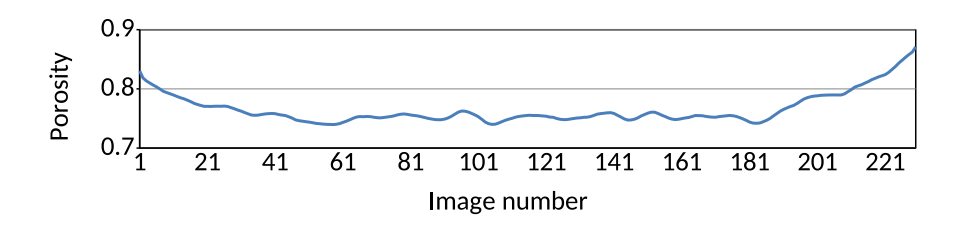


Fig. 6. Porosity of the image layers 1 to 230 of geometry \mathcal{O} .

Table 3. Tortuosity τ and permeability κ of the stochastic geometries. The in-plane direction 1 is the y direction of the modeled fiber bundles in cases A-F. The in-plane permeabilities of the 10% and 20% compression of case F were used for the confirmation of the rotation angle α in section 5.2.

No.	Compression	Through-plane		In-plane 1		In-plane 2		Rotated		
		au	κ_0	au	κ_y	au	κ_z	κ_a	κ_b	κ_a/κ_b
	/ %		$/\ \mu m^2$		$/\ \mu m^2$		$/\ \mu m^2$	$/\ \mu m^2$	$/\ \mu m^2$	
О	0	1.208	6.24	1.160	8.52	1.150	8.79	_	_	_
A	0	1.210	10.18	1.139	14.51	1.174	10.73	13.86	11.38	1.22
В		1.217	9.35	1.143	13.87	1.178	10.98	13.73	11.48	1.20
\mathbf{C}		1.211	10.01	1.132	15.22	1.170	11.56	14.59	12.19	1.20
D		1.218	9.56	1.137	14.94	1.183	10.87	14.24	11.57	1.23
E		1.203	9.67	1.148	13.28	1.179	11.07	12.90	11.45	1.13
\mathbf{F}		1.212	9.82	1.139	14.41	1.173	11.67	13.94	12.14	1.15
A	30	1.233	5.02	1.193	5.99	1.248	3.57	5.57	3.99	1.40
В		1.246	4.59	1.198	5.54	1.256	3.62	5.21	3.95	1.32
\mathbf{C}		1.226	5.09	1.180	6.34	1.244	3.91	5.92	4.33	1.38
D		1.237	4.99	1.185	6.00	1.259	3.63	5.59	4.04	1.38
\mathbf{E}		1.224	4.70	1.213	5.05	1.277	3.81	4.84	4.02	1.20
\mathbf{F}		1.241	4.93	1.195	5.68	1.245	4.16	5.42	4.42	1.23
F	0	1.212	9.82	1.139	14.41	1.173	11.67	13.94	12.14	1.15
	10	1.208	8.99	1.153	11.32	1.191	8.94	10.91	9.35	1.17
	20	1.224	6.87	1.170	8.40	1.213	6.45	8.06	6.79	1.19
	30	1.241	4.93	1.195	5.68	1.245	4.16	5.42	4.42	1.23
average	0		9.77		14.37		11.15	13.82	11.70	1.18
A-F	30		4.88		5.77		3.78	5.43	4.12	1.32

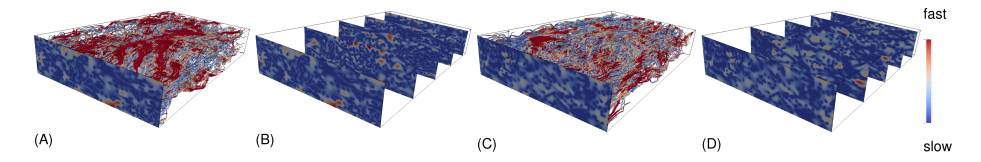


Fig. 7. Flow distribution of gas transport, y (in-plane 1) direction; the fibers of the micro structure are not visualized: (A) geometry O, uncompressed, flow lines colored with velocity magnitude; (B) distribution of y velocity corresponding to sample in; (C) geometry F, in-plane along fiber bundles, 10% compression, flow lines colored with velocity magnitude; (D) distribution of y velocity corresponding to sample in C.

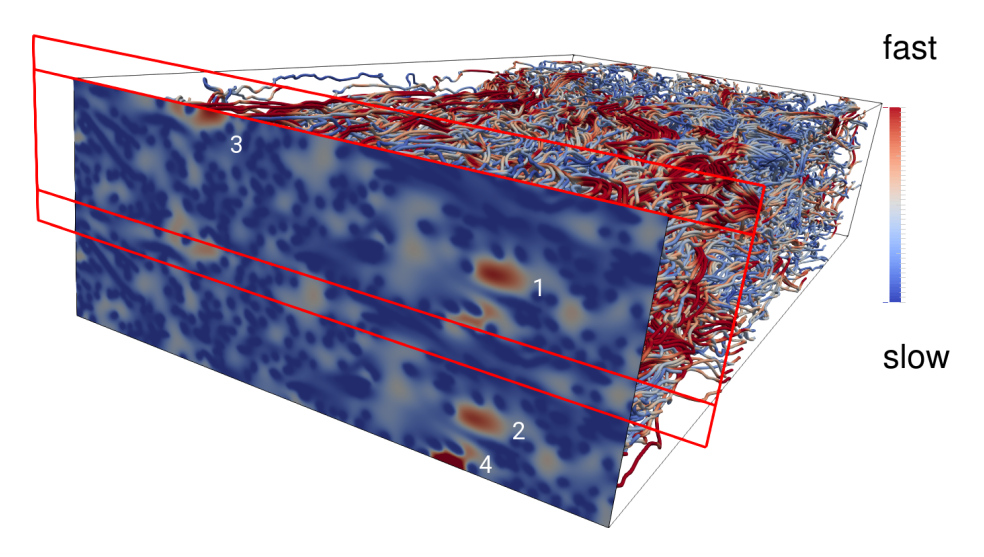


Fig. 8. Flow distribution of gas transport, y (in-plane 1) direction, stack of two layers of the inner region of geometry O; red frame: region displayed in Fig. 7 (A) and the omitted outer regions. The fibers of the micro structure are not visualized.

Table 4. In-plane tortuosity τ and permeability κ of the inner section of the original geometry.

No.	Compression	In-plane 1		In-plane 2	
		au	κ_y	au	κ_z
	%		μm^2		μm^2
O (core)	0++	1.163	6.75	1.163	6.36